




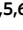








A comparison of microfluidic methods for high-throughput cell deformability measurements

Marta Urbanska ^{1,10}, Hector E. Muñoz ^{2,10}, Josephine Shaw Bagnall ³, Oliver Otto ^{1,4},
Scott R. Manalis ^{3,5,6} , Dino Di Carlo ^{2,7,8}  and Jochen Guck ^{1,9} 

The mechanical phenotype of a cell is an inherent biophysical marker of its state and function, with many applications in basic and applied biological research. Microfluidics-based methods have enabled single-cell mechanophenotyping at throughputs comparable to those of flow cytometry. Here, we present a standardized cross-laboratory study comparing three microfluidics-based approaches for measuring cell mechanical phenotype: constriction-based deformability cytometry (cDC), shear flow deformability cytometry (sDC) and extensional flow deformability cytometry (xDC). All three methods detect cell deformability changes induced by exposure to altered osmolarity. However, a dose-dependent deformability increase upon latrunculin B-induced actin disassembly was detected only with cDC and sDC, which suggests that when exposing cells to the higher strain rate imposed by xDC, cellular components other than the actin cytoskeleton dominate the response. The direct comparison presented here furthers our understanding of the applicability of the different deformability cytometry methods and provides context for the interpretation of deformability measurements performed using different platforms.

The mechanical phenotype of cells is a valuable indicator of changes in their internal structure and is tightly associated with cell state and function^{1–3}. Alterations in the mechanical properties of cells have been linked to processes such as cell cycle progression⁴, cancer malignancy^{5–8}, leukocyte activation^{9–13} and stem cell differentiation^{11,14–16}. Measurements of cell mechanics circumvent the need for extrinsic labels, such as fluorescent dyes, and therefore constitute an attractive noninvasive biomarker for cell identification. Furthermore, as cell mechanical phenotypes determine the magnitude of the mechanical response of cells to environmental forces, cell mechanics can provide a biophysical perspective on cellular processes, such as vascular circulation or migration during development and metastasis^{17,18}.

Methods such as atomic force microscopy¹⁹, micropipette aspiration²⁰, optical stretching²¹ and parallel-plate rheology²² are used to quantify deformation of single cells under exposure to external stresses, and they have been compared in detail with a broader range of methods in a recent publication²³. These methods evaluate time-resolved responses to force and enable extraction of physical properties, such as elastic modulus or viscosity. They suffer, however, from technically demanding and time-consuming procedures that limit measurement throughput and the uptake of these techniques beyond specialized laboratories. Microfluidics-based approaches constitute an attractive alternative³. They allow robust, high-throughput assessment of the ability of cells to change shape under applied forces—their deformability—and enable thorough characterization of homogeneous and heterogeneous cell populations. Moreover, due to the ease of handling, these approaches have the potential to be implemented in both biological laboratories and clinical settings.

The currently available microfluidics-based deformability cytometry methods vary in type and magnitude of applied stress, the rate at which cells are deformed and the way deformability is parameterized. One major class, cDC, relies on driving cells through a constriction smaller than their diameter and measuring the time needed for cells to pass through the constriction^{7,13,24–26}. The translocating cells are detected by means of optical imaging^{13,25,26}, electrical resistance measurements²⁴ or mechanical frequency changes of a suspended microchannel resonator (SMR)⁷. The deformability of the cells is typically deduced directly from their passage time; however, in some variations of the method, additional image-based evaluation of cell deformation over time is performed and viscoelastic cell properties are extracted^{25,26}. The remaining classes of deformability cytometry employ hydrodynamic flow to induce cell deformation in a contactless manner and infer cell deformability from image-based evaluation of cell shape. One class of such contactless methods, sDC, employs shear stress and pressure gradients in a long, narrow channel to deform cells into a bullet-like shape within a few milliseconds. An example of this class constitutes real-time deformability cytometry (RT-DC)⁴, which operates at strain rates of the order of 0.1 kHz. Another class of contactless methods, xDC, uses an extensional flow usually associated with a cross-slot microfluidic architecture. A representative of this class is deformability cytometry (DC)¹¹, typically operating at high strain rates of the order of 10 kHz. By increasing the viscosity of the measuring buffer and lowering flow rates, xDC can be adjusted to operate at lower strain rates (<2 kHz)^{27,28}. Variabilities in the mode and timescales of operation, types of samples analyzed and preparation conditions render it challenging to compare the published results obtained with different deformability cytometry methods. Despite substantial work

¹Biotechnology Center, Center for Molecular and Cellular Bioengineering, Technische Universität Dresden, Dresden, Germany. ²Department of Bioengineering, University of California, Los Angeles, Los Angeles, CA, USA. ³Department of Biological Engineering, Massachusetts Institute of Technology, Cambridge, MA, USA. ⁴Zentrum für Innovationskompetenz: Humorale Immunreaktionen in kardiovaskulären Erkrankungen, Universität Greifswald, Greifswald, Germany. ⁵Department of Mechanical Engineering, Massachusetts Institute of Technology, Cambridge, MA, USA. ⁶Koch Institute for Integrative Cancer Research, Massachusetts Institute of Technology, Cambridge, MA, USA. ⁷California NanoSystems Institute, University of California, Los Angeles, Los Angeles, CA, USA. ⁸Jonsson Comprehensive Cancer Center, University of California, Los Angeles, Los Angeles, CA, USA. ⁹Max Planck Institute for the Science of Light and Max-Planck-Zentrum für Physik und Medizin, Erlangen, Germany. ¹⁰These authors contributed equally: Marta Urbanska, Hector E. Muñoz. ✉e-mail: srm@mit.edu; dicarlo@ucla.edu; jochen.guck@mpl.mpg.de

on identifying cellular structures that contribute to deformability changes with individual methods^{4,7,11,16,29}, a direct comparison of the performance of the different methods is still missing.

To close this gap, we performed a standardized cross-laboratory study comparing representatives of the three deformability cytometry classes: (1) an SMR-based cDC variant⁷, (2) RT-DC⁴ as an example of sDC and (3) DC¹¹ as an example of xDC. With these methods, we evaluated deformability of human promyelocytic leukemia (HL60) cells—from the same source and passage number—in two standardized assays, subjecting the cells to osmotic changes and to latrunculin B-induced actin disassembly. Our results show that deformability is altered by osmotic changes in all three of the methods presented. In contrast, the deformability increase due to actin disassembly is detectable with cDC and sDC, but not with the xDC method implemented in this study. The direct comparison presented here provides context for the interpretation of deformability measurements performed with different high-throughput microfluidics-based techniques for measuring cell mechanics that operate at different strain rates and different stress magnitudes.

Results

Microfluidics-based methods to assess cell deformability. In this work we compare representatives of cDC, sDC and xDC. To minimize the influence of potential biological variability, the three participating laboratories shared a common stock of the HL60 cell subline (HL60/S4) and performed measurements within ten passages upon receipt. To further standardize the growth conditions, we used the same serum lot, followed the same subculturing protocol and collected the cells for measurements at a specified culture concentration range ($0.5\text{--}1 \times 10^6$ cells per ml of culture). In our study, cDC refers to an SMR-based variant using a fluidic microchannel embedded in a silicon microcantilever⁷. Close to the cantilever apex, the microchannel features a constriction smaller than the cell size ($6\ \mu\text{m}$ wide, $15\ \mu\text{m}$ high and $50\ \mu\text{m}$ long; Fig. 1a). Cells are driven through this constriction by a constant pressure of 1 kPa, and deform upon contact with the channel walls. The time it takes the cell to enter and pass through the constriction is assessed using changes in the resonance frequency of the microcantilever (Fig. 1a). In cDC, cell deformability, D , is defined as the inverse of cell passage time (Fig. 1a). The characteristic passage time of untreated HL60 cells was 23 ms (Supplementary Fig. 1), with a throughput of a few cells per second and a strain rate of 0.04 kHz.

sDC and xDC (here referring to RT-DC⁴ and DC¹¹, respectively) both rely on hydrodynamic flow to deform cells in a contactless manner, and on high-speed imaging to assess the ensuing cell deformation. Yet, they operate using different channel geometries, and, more importantly, different probing timescales and Reynolds numbers (Table 1). The dimensionless Reynolds number ($\text{Re} = \frac{\rho v L}{\eta}$, where ρ is the fluid density, v the mean flow velocity, L the characteristic length of the flow system and η the dynamic viscosity of the fluid), expresses the relative importance of inertial versus viscous forces and is equal to 0.4 for sDC and 150 for xDC. The low Re in the case of sDC ($\ll 1$) indicates a dominance of viscous forces, where the motion of the cells through the liquid leads to normal and shear forces that deform the cell. xDC, in turn, operates in an inertial flow regime, where the forces that result from the rapid acceleration or deceleration of cells and fluid also play a role in cell deformation. In addition, inertial forces can lead to other useful effects, such as cell focusing³⁰, which is leveraged in xDC to align cells such that they experience more consistent forces during deformation.

In sDC, cells are driven through a funnel-like constriction into a $\sim 300\text{-}\mu\text{m}$ -long microfluidic channel, at the end of which they reach a steady-state cell deformation, defined as $1 - \text{circularity}$ (Fig. 1b). Cells take a few milliseconds to travel through the channel and the strain is induced at a rate of 0.2 kHz. Typically, over 100 cells per second can be analyzed. For HL60 cells, we used chips with a

square channel cross-section of $20 \times 20\ \mu\text{m}^2$, which, together with hydrodynamic focusing implemented upstream of the deformation channel, assures that cells are not in contact with the channel walls. The stress acting on the cells during sDC measurements reaches values of the order of 1 kPa (Supplementary Note 1).

In xDC, cells are stretched by an extensional flow in a cross-junction of a microfluidic chip (Fig. 1c). The cells are delivered to the cross-junction at a speed of several meters per second, where they are fully decelerated and deformed via inertial forces within a few microseconds. This allows for analysis rates of over 1,000 cells per second. Cell size is determined from images recorded before the cell extension, and deformability, D , is defined as the maximal aspect ratio observed in the extensional flow region. The channels of the xDC chip have a rectangular cross-section of $60 \times 30\ \mu\text{m}^2$. Before entry to the analysis region, cells are aligned via inertial focusing, and do not interact with the channel walls. Compared to sDC and cDC, xDC applies several-fold higher stress to the cells, and reaches a relatively high strain rate of 20 kHz (Table 1 and Supplementary Note 1).

The raw data obtained with all three methods are typically displayed on a scatter plot of deformability versus cell diameter (Fig. 1). Hallmark parameters of the operation of cDC, sDC and xDC are summarized in Table 1.

Osmotic shock-induced deformability changes are detectable consistently across methods. To compare the deformability measurements among cDC, sDC and xDC, we first performed a series of osmotic shock experiments on HL60 cells. In hyperosmotic solutions water is driven out of cells (Fig. 2a), leading to a decrease in cell size and increased molecular crowding inside the cell, which has been linked to elevated cell stiffness^{31–34}. On the contrary, in hypo-osmotic conditions water enters the cells to compensate for the osmolyte concentration difference, leading to cell swelling, dilution of intracellular material (Fig. 2a) and a decrease in cell stiffness^{31,33}.

To induce an osmotic shock response, we altered the osmolarity of the buffer with respect to the HL60 physiological osmolarity of 300 mOsm, which is characteristic for human blood plasma³⁵. We prepared the hyperosmotic solutions with osmolarities ranging from 400 to 700 mOsm by adding mannitol to the measurement buffer, and the hypo-osmotic solutions with osmolarities of 250 and 200 mOsm by diluting the measurement buffer with water. We exposed cells to altered osmolarity for 10 min before measurements. Consistently across the three methods, the hyperosmotic conditions caused a decrease in cell size and deformability, while hypo-osmotic conditions caused an increase of both parameters (Fig. 2b–d and Supplementary Figs. 2 and 3). Since the observed deformability response to hypo-osmotic shock shows nonmonotonic evolution over time (Supplementary Fig. 4), we excluded the hypo-osmotic conditions from further analysis.

To facilitate the comparison of deformabilities measured with the individual methods, we introduced relative deformability, RD, calculated with respect to the control conditions (Methods and Supplementary Fig. 3). We fitted the relationships between RD and the normalized extracellular osmolarity upon hyperosmotic shock for each method with an exponential curve (Fig. 2e and Supplementary Table 1) with the following formula: $\text{RD} = e^{\lambda(1 - \text{Osm}/\text{Osm}_{\text{iso}})}$, where λ is the decay constant that describes the sensitivity of RD to the change in the osmolarity, Osm , normalized to the iso-osmotic condition, Osm_{iso} . The exponential fits provide the best description of the obtained results, as compared to linear and power law fits (Supplementary Fig. 5).

Although all three methods follow the same exponential trend of decreasing RD with increasing osmolarity, the decay constants, λ , differ. This is confirmed by the results of pairwise F -tests, which show that there is a significant difference between the cDC and

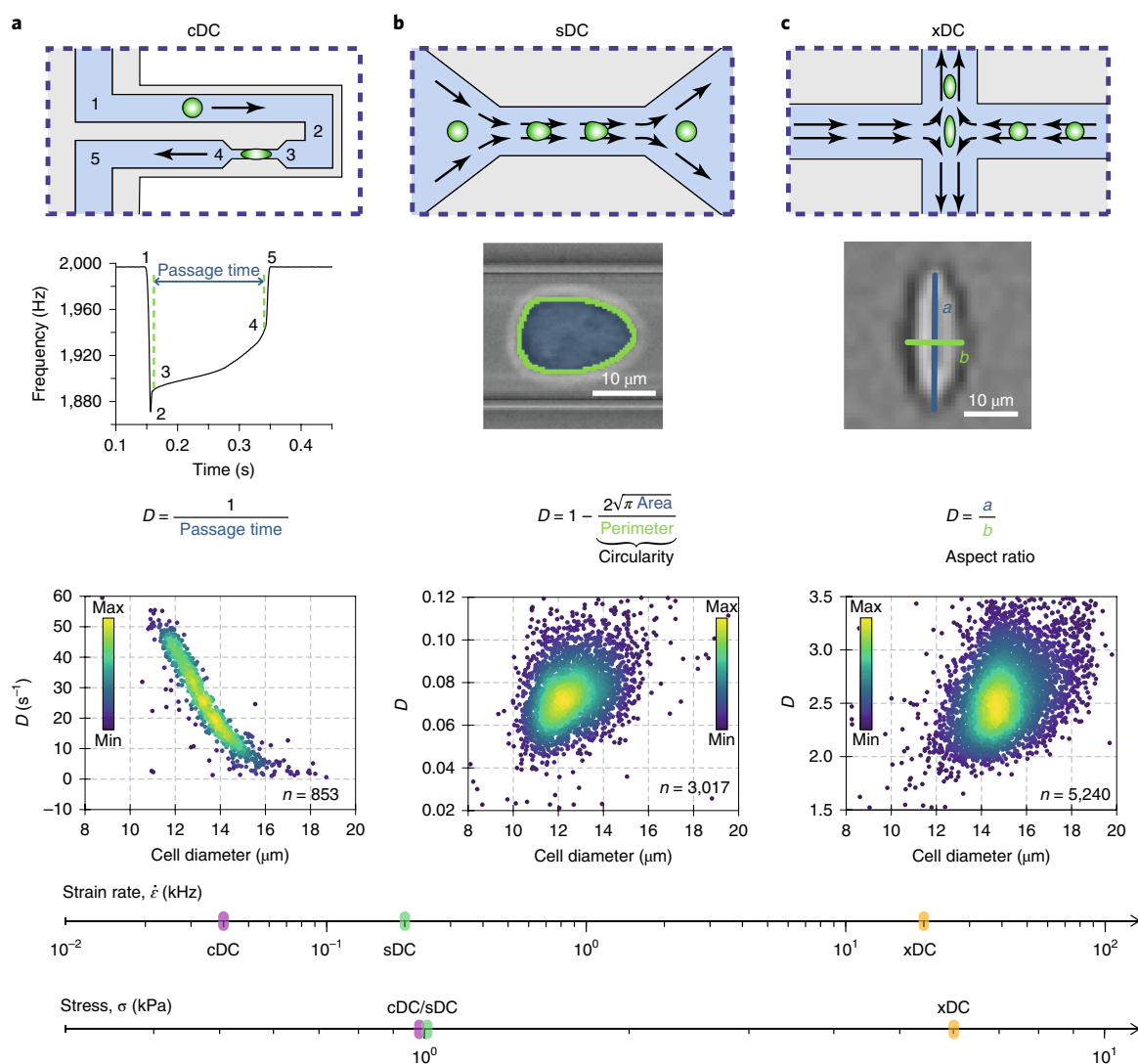


Fig. 1 | Comparison of the microfluidics-based approaches for the determination of cell deformability used in this study. **a–c**, Operation principle of cDC (**a**), sDC (**b**) and xDC (**c**). Schematic representation of the chip geometries used in the respective methods (top row). Overview of how the deformability, D , is defined for each method (middle row). The numbers 1–5 in the plot of frequency versus time correspond to the cell positions in the cDC microchannel indicated in the scheme above. Representative scatter plots of D versus cell diameter from the measurements of untreated HL60 cells (bottom row); n indicates number of cells; the measurements were repeated a total of 10, 9 and 8 times for cDC, sDC and xDC, respectively. The color map corresponds to event density. The strain rate and stress applied to the cells in cDC, sDC and xDC are indicated on the corresponding axes at the bottom of the panel.

xDC curves ($F_{1,35} = 70.6$, $P = 6.5 \times 10^{-10}$), cDC and sDC curves ($F_{1,35} = 29.8$, $P = 3.9 \times 10^{-6}$), as well as between sDC and xDC curves ($F_{1,38} = 89.6$, $P = 1.5 \times 10^{-11}$). The sensitivity of the exponential decay, λ , is highest for cDC, reaching values that are 1.5 and 3 times higher than those obtained for sDC and xDC, respectively (Supplementary Table 1).

Ability to detect actin disassembly is method dependent. To further interrogate the differences in deformability measurements between cDC, sDC and xDC, we compared their performance in detecting actin disassembly induced by latrunculin B (LatB). The actin cytoskeleton contributes to cell mechanics at low strains, and its destabilization with chemical agents reduces cell stiffness^{26–29,36}. In suspended cells, actin filaments are predominantly organized into an actin cortex—a thin, cross-linked network underlying the plasma membrane³⁷. LatB binds free actin monomers (G-actin), thereby inhibiting actin polymerization and destabilizing filamentous actin structures (F-actin), such as the actin cortex, in a dose-dependent manner^{38,39} (Fig. 3a).

We treated HL60 cells with a range of LatB concentrations (1–100 ng ml⁻¹, corresponding to 2.53–253 nM), along with a DMSO vehicle control, and performed deformability measurements with cDC, sDC and xDC (Fig. 3b–d). As revealed by analysis of variance, LatB treatment had a significant effect on the cell deformability as measured with cDC ($F_{6,16} = 17.2$, $P = 3.6 \times 10^{-6}$) and sDC ($F_{6,28} = 34.3$, $P = 1.2 \times 10^{-11}$). In contrast, the xDC measurements did not reveal significant deformability changes upon LatB treatment ($F_{6,21} = 0.38$, $P = 0.89$), although we observed a subtle deformability decrease at the highest LatB concentration (100 ng ml⁻¹; Fig. 3d,e and Supplementary Fig. 6c,f,i). When we used an increased flow rate in sDC, cell deformability reached its maximum at 50 ng ml⁻¹ LatB concentration and showed a decline at 100 ng ml⁻¹ (Supplementary Fig. 7a). Additionally, with increased flow rate the overall magnitude of the RD response showed a decrease (Supplementary Fig. 7b). Increase of LatB concentration beyond 100 ng ml⁻¹ caused decrease of deformability as observed with cDC and sDC (Supplementary Fig. 8), consistent with the trend observed previously with xDC¹¹. For all three methods, cell

Table 1 | Operation parameters of cDC, sDC and xDC

	cDC	sDC	xDC
Deformability measure	(Passage time) ⁻¹	1 – circularity	Aspect ratio
Detection	Frequency shift	Imaging	Imaging
Analysis	Offline	Real time	Offline
Throughput (cells s ⁻¹)	1	100	1,000
Timescale of cell deformation, τ (ms)	10	1	0.01
Cell contact with channel walls	Yes	No	No
Channel width \times height (μm)	6 \times 15	20 \times 20	60 \times 30
Mean flow velocity, v (m s ⁻¹)	0.01	0.1	3.5
Viscosity of measuring buffer, η (mPa s ⁻¹)	1	5.7	1
Re number in the measuring channel	0.1	0.4	150
Mean absolute strain, $\bar{\epsilon}$	37%	17%	24%
Strain rate, $\dot{\epsilon}$ (kHz)	0.04	0.2	20
Applied stress, σ (kPa)	~ 1	-1	-6

size remained fairly constant at low LatB concentrations. However, at LatB concentrations of 50 ng ml⁻¹ and 100 ng ml⁻¹ the determined cell size decreased slightly (Supplementary Fig. 9).

For cDC and sDC, the change of RD in response to increasing LatB concentration exhibited a sigmoidal dose–response behavior, while xDC data did not follow such trend (Fig. 3e and Supplementary Table 2). The half-maximal effective concentration, EC₅₀, reached 11.9 ng ml⁻¹ for cDC and 14.9 ng ml⁻¹ for sDC. The upper RD response limit was also similar for these two methods, with 1.46 for cDC and 1.52 for sDC. Concurrently, as revealed by the pairwise *F*-test, there was no significant difference between the obtained cDC and sDC fits ($F_{4,50} = 0.6$, $P = 0.69$), whereas we found significant differences between cDC and xDC curves ($F_{4,43} = 44.3$, $P = 1.0 \times 10^{-14}$), as well as between sDC and xDC curves ($F_{4,55} = 63.7$, $P = 5.3 \times 10^{-20}$).

Discussion

Integrating mechanical characterization into the current view of cellular behavior paves the way toward a more comprehensive understanding of physiological and pathological processes^{17,18} with potential clinical diagnostic value^{1,2,8,12,40}. Establishment and validation of methods measuring the mechanical properties of cells is providing grounds for further developments in the field. In a recent publication²³, elastic and viscous moduli of a standardized cell line were measured with several traditional techniques, revealing a spread of obtained values over several orders of magnitude. This variability was attributed to the magnitude of applied stress and strain rate, probe size, probing length scale and whether the cells were attached or in suspension. Here, we complemented this analysis by performing a cross-laboratory comparison of three widely used microfluidic cell deformability measurement techniques, cDC, sDC and xDC. While applying different strain rates and stresses, all three methods probe whole-cell deformation in a suspended cell state, which reduces potential sources of variability.

All three techniques consistently measured an exponential decrease of deformability with increasing osmolarity, albeit with varying sensitivity. The change in cell volume induced by osmotic shock leads to a multifaceted change in the internal structure, not only within the cytoplasm, but also in the cell nucleus⁴¹. Although the osmotic response can trigger changes in the relative F-actin content⁴² and actin cytoskeleton structure³¹, the overall changes in mechanical properties were shown to be actin independent and attributed mostly to macromolecular crowding inside the cell³². We therefore conclude that the density of packing of the colloidal

fraction inside the cell induces deformability changes that are detectable across all tested methods.

The discrepancies in deformability changes upon actin destabilization can likely be attributed to the difference in applied strain rates. cDC and sDC induce similar strain rates and show an almost identical change in the measured deformabilities upon actin destabilization. xDC, on the other hand, applies a higher strain rate and has been previously reported not to measure responses to actin cytoskeletal perturbations¹¹, presumably due to fluidization of actin networks observed at high strain magnitudes and strain rates^{43,44}. This is further supported by the fact that adapting xDC to operate at lower strain rates enables detection of deformability changes upon disruption of actin cytoskeleton in cells^{27,28} and by the decreased dynamic range of the relative deformability response when using increased flow rates in sDC. Upon strong destabilization of the actin cytoskeleton resulting in substrate detachment of adherent cells^{11,38}, the cells exhibit a reduction of deformability, indicating a biphasic nature for the cell mechanical response to actin disassembly.

In addition to measuring cell deformability, each of the presented methods features a set of distinct functionalities that expand the dimensionality of the performed measurements. The SMR-based cDC provides additional parameters describing cell passage through the constriction, such as entry and transit velocities, and enables a sensitive readout of cell buoyant mass^{7,45}. sDC stands out with its real-time data processing, which renders the method compatible with active sorting downstream of deformability analysis⁴⁶. Moreover, for sDC an integrated fluorescence-activated cell sorting (FACS)-like readout of cell and cell compartment fluorescence is available⁴⁷, as well as a theoretical framework allowing for the extraction of Young's moduli from the deformability data^{48,49}. Recently developed dynamic RT-DC enables assignment of viscosity to measured cells by analyzing the time evolution of cell deformation in the channel⁵⁰. xDC surpasses cDC and sDC in its throughput. Finally, in all techniques bright-field cell images are collected and can be used for extraction of additional image-based features for further cell characterization.

In the light of our results, we recommend the use of cDC or sDC when probing cellular changes involving the actin cytoskeleton, and all three methods when changes in cytoplasmic packing induced by osmotic shock are at play. Since cDC is the only method that involves physical contact of cells with the channel walls, we recommend this method for studies in which cell friction or retention, in processes such as microcirculation, is of interest. xDC, in turn,

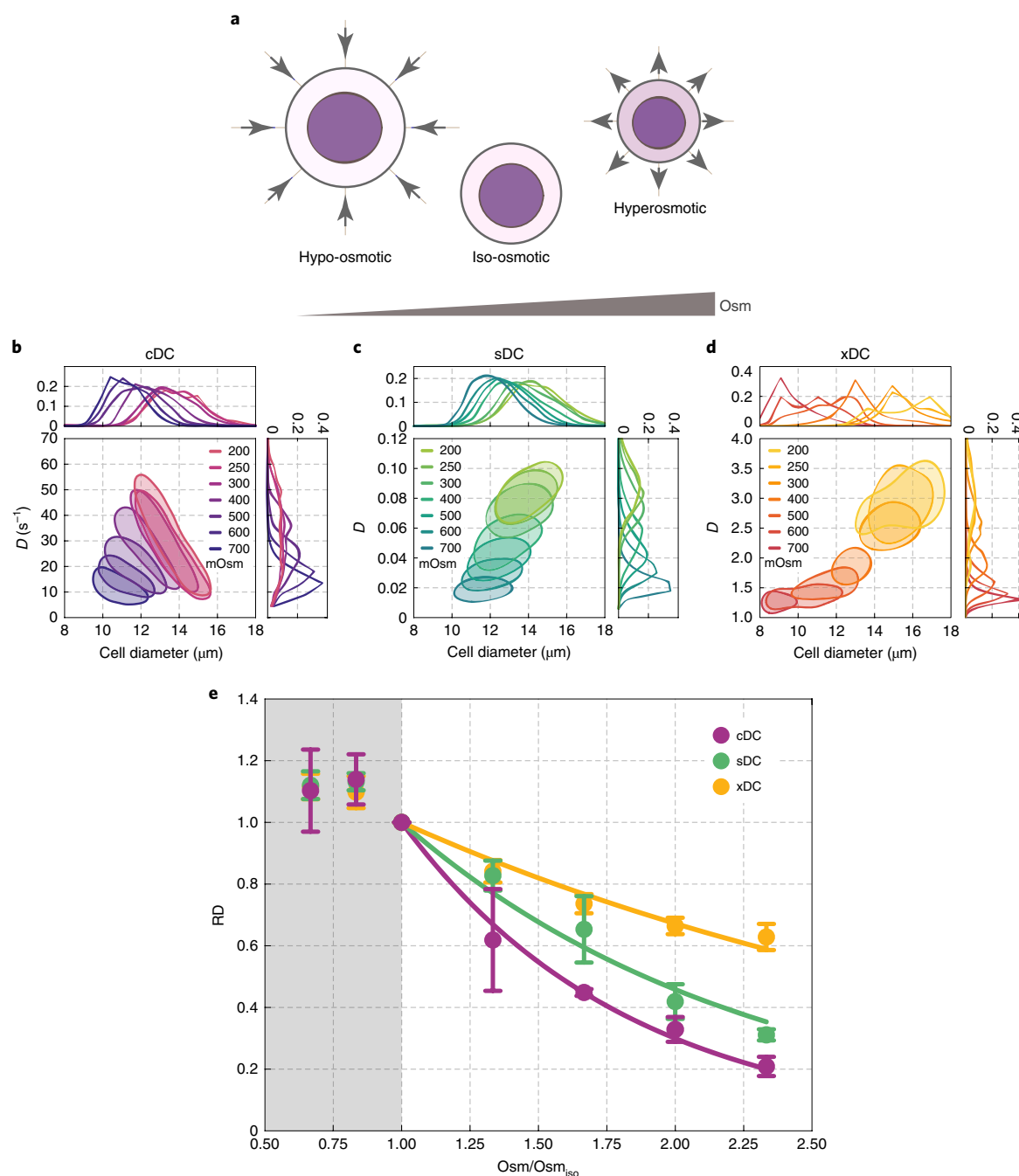


Fig. 2 | Effects of osmolarity changes on cell deformability. **a**, Extracellular osmolarity when decreased beyond physiological (iso-osmotic) conditions causes cell swelling and dilution of intracellular material, whereas an increase of extracellular osmolarity results in cell shrinkage and an increase in macromolecular crowding inside the cell. Arrows indicate the direction of water flow. **b–d**, Deformability changes upon osmolarity treatment observed in exemplary cDC (**b**), sDC (**c**) and xDC (**d**) experiments. Contour plots (50% density) of deformability, D , versus cell diameter for HL60 cells treated with increasing osmolarity are accompanied by deformability and cell diameter histograms. **e**, RD as a function of normalized osmolarity, Osm/Osm_{iso} , for cDC (purple), sDC (green) and xDC (yellow) measurements. Data points represent means of medians of multiple experimental replicates ($n=3, 4$ and 4 , for cDC, sDC and xDC, respectively), and error bars represent standard deviation. Lines represent exponential fits to data. Hypo-osmotic shock data excluded from the fitting procedure are shaded in gray.

was previously shown to provide a readout of changes in structures localized deeper in the cells, such as the nucleus¹¹. For further reference, a comprehensive overview of studies performed using the different deformability cytometry classes is presented in Supplementary Table 3.

Taken together, the comparison study presented here aids the understanding of the strengths and limitations of deformability

cytometry methodologies, provides context for interpreting deformability measurements across various platforms and fosters cell deformability as a metric for mechanophenotyping at high throughputs⁵¹.

Online content

Any methods, additional references, Nature Research reporting summaries, source data, extended data, supplementary information,

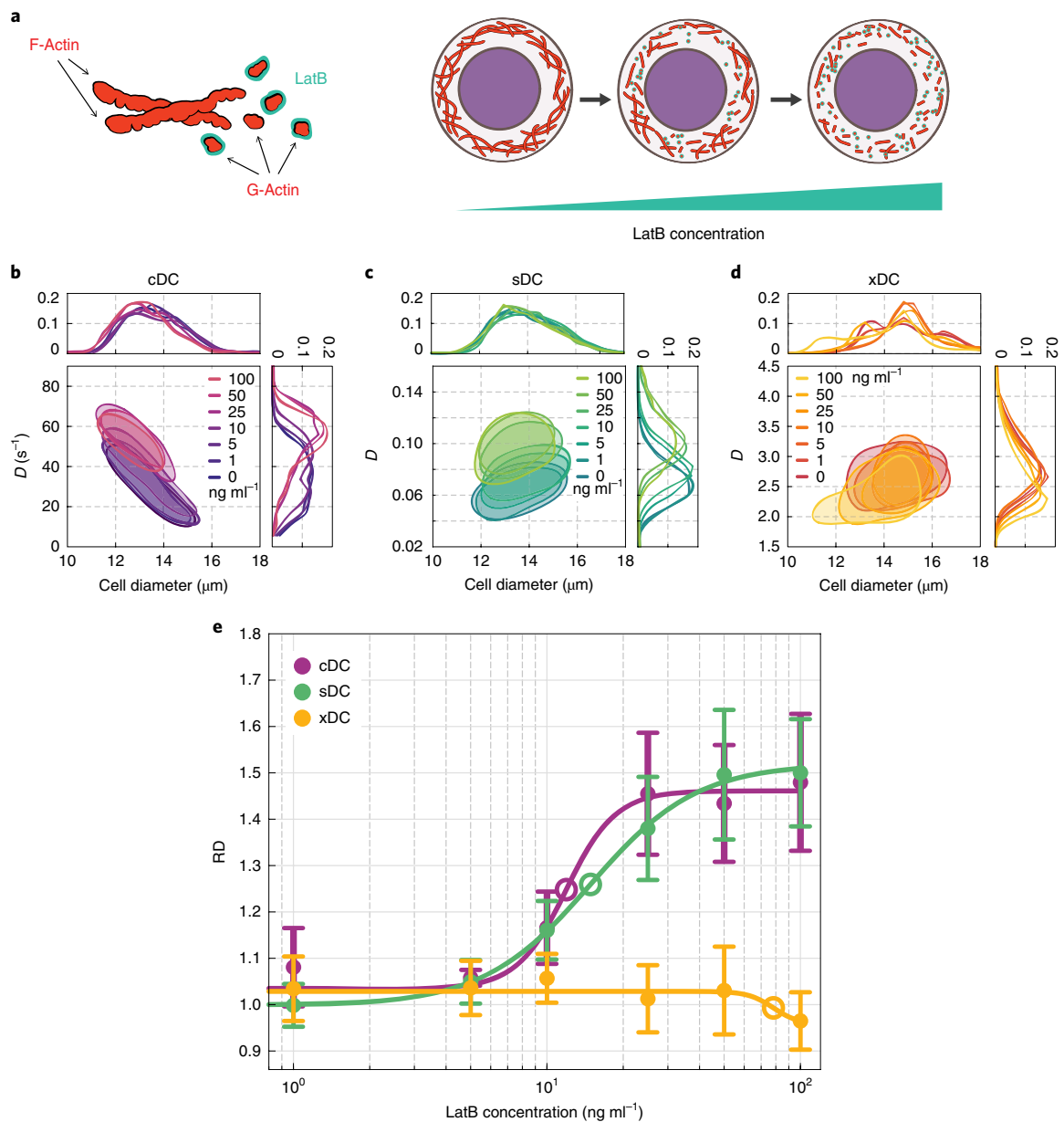


Fig. 3 | Effects of LatB-induced actin disassembly on cell deformability. **a**, LatB causes dose-dependent disassembly of actin cytoskeleton by scavenging actin monomers. **b–d**, Deformability changes of HL60 cells upon LatB treatment observed in exemplary cDC (**b**), sDC (**c**) and xDC (**d**) experiments. Contour plots (50% density) of deformability, D , versus cell diameter for HL60 cells treated with increasing dose of LatB are accompanied by deformability and cell diameter histograms. **e**, RD as a function of LatB dose for cDC (purple), sDC (green) and xDC (yellow) measurements (closed circles). Data points represent means of medians of multiple experiment replicates ($n=3$, 5 and 4, for cDC, sDC and xDC, respectively), and error bars represent standard deviation. Lines are four-parameter log-logistic fits, with LatB EC₅₀ values indicated with open circles.

acknowledgements, peer review information; details of author contributions and competing interests; and statements of data and code availability are available at <https://doi.org/10.1038/s41592-020-0818-8>.

Received: 7 April 2019; Accepted: 23 March 2020;
Published online: 27 April 2020

References

- Di Carlo, D. A mechanical biomarker of cell state in medicine. *J. Lab. Autom.* **17**, 32–42 (2012).
- Nematbakhsh, Y. & Lim, C. T. Cell biomechanics and its applications in human disease diagnosis. *Acta Mech. Sin.* **31**, 268–273 (2015).
- Darling, E. M. & Di Carlo, D. High-throughput assessment of cellular mechanical properties. *Annu. Rev. Biomed. Eng.* **17**, 35–62 (2015).
- Otto, O. et al. Real-time deformability cytometry: on-the-fly cell mechanical phenotyping. *Nat. Methods* **12**, 199–202 (2015).
- Guck, J. et al. Optical deformability as an inherent cell marker for testing malignant transformation and metastatic competence. *Biophys. J.* **88**, 3689–3698 (2005).
- Swaminathan, V. et al. Mechanical stiffness grades metastatic potential in patient tumor cells and in cancer cell lines. *Cancer Res.* **71**, 5075–5080 (2011).
- Byun, S. et al. Characterizing deformability and surface friction of cancer cells. *Proc. Natl Acad. Sci. USA* **110**, 7580–7585 (2013).
- Tse, H. T. K. et al. Quantitative diagnosis of malignant pleural effusions by single-cell mechanophenotyping. *Sci. Transl. Med.* **5**, 212ra163 (2013).

9. Bufi, N. et al. Human primary immune cells exhibit distinct mechanical properties that are modified by inflammation. *Biophys. J.* **108**, 2181–2190 (2015).
10. Bashant, K. R. et al. Real-time deformability cytometry reveals sequential contraction and expansion during neutrophil priming. *J. Leukoc. Biol.* **105**, 1143–1153 (2019).
11. Gossett, D. R. et al. Hydrodynamic stretching of single cells for large population mechanical phenotyping. *Proc. Natl Acad. Sci. USA* **109**, 7630–7635 (2012).
12. Toepfner, N. et al. Detection of human disease conditions by single-cell morpho-rheological phenotyping of blood. *eLife* **7**, e29213 (2018).
13. Rosenbluth, M. J., Lam, W. A. & Fletcher, D. A. Analyzing cell mechanics in hematologic diseases with microfluidic biophysical flow cytometry. *Lab Chip* **8**, 1062–1070 (2008).
14. Ekpenyong, A. E. et al. Viscoelastic properties of differentiating blood cells are fate- and function-dependent. *PLoS ONE* **7**, e45237 (2012).
15. Urbanska, M. et al. Single-cell mechanical phenotype is an intrinsic marker of reprogramming and differentiation along the mouse neural lineage. *Development* **144**, 4313–4321 (2017).
16. Lin, J. et al. High-throughput physical phenotyping of cell differentiation. *Microsyst. Nanoeng.* **3**, 17013 (2017).
17. Mammoto, T. & Ingber, D. E. Mechanical control of tissue and organ development. *Development* **137**, 1407–1420 (2010).
18. Chan, C. J., Heisenberg, C. P. & Hiiragi, T. Coordination of morphogenesis and cell-fate specification in development. *Curr. Biol.* **27**, R1024–R1035 (2017).
19. Radmacher, M. Studying the mechanics of cellular processes by atomic force microscopy. *Methods Cell Biol.* **83**, 347–372 (2007).
20. Hochmuth, R. M. Micropipette aspiration of living cells. *J. Biomech.* **33**, 15–22 (2000).
21. Guck, J. et al. The optical stretcher: a novel laser tool to micromanipulate cells. *Biophys. J.* **81**, 767–784 (2001).
22. Thoumine, O., Ott, A., Cardoso, O. & Meister, J.-J. Microplates: a new tool for manipulation and mechanical perturbation of individual cells. *J. Biochem. Biophys. Methods* **39**, 47–62 (1999).
23. Wu, P. H. et al. A comparison of methods to assess cell mechanical properties. *Nat. Methods* **15**, 491–498 (2018).
24. Adamo, A. et al. Microfluidics-based assessment of cell deformability. *Anal. Chem.* **84**, 6438–6443 (2012).
25. Lange, J. R. et al. Microconstriction arrays for high-throughput quantitative measurements of cell mechanical properties. *Biophys. J.* **109**, 26–34 (2015).
26. Nyberg, K. D. et al. Quantitative deformability cytometry: rapid, calibrated measurements of cell mechanical properties. *Biophys. J.* **113**, 1574–1584 (2017).
27. Guillou, L. et al. Measuring cell viscoelastic properties using a microfluidic extensional flow device. *Biophys. J.* **111**, 2039–2050 (2016).
28. Armistead, F. J., De Pablo, J. G., Gadêlha, H., Peyman, S. A. & Evans, S. D. Cells under stress: an inertial-shear microfluidic determination of cell behaviour. *Biophys. J.* **4**, 1127–1135 (2019).
29. Golfier, S. et al. High-throughput cell mechanical phenotyping for label-free titration assays of cytoskeletal modifications. *Cytoskeleton* **74**, 283–296 (2017).
30. Di Carlo, D. Inertial microfluidics. *Lab Chip* **9**, 3038 (2009).
31. Guilak, F., Erickson, G. K. & Ting-Beall, H. P. The effects of osmotic stress on the viscoelastic and physical properties of articular chondrocytes. *Biophys. J.* **82**, 720–727 (2002).
32. Zhou, E. H. et al. Universal behavior of the osmotically compressed cell and its analogy to the colloidal glass transition. *Proc. Natl Acad. Sci. USA* **106**, 10632–10637 (2009).
33. Moeendarbary, E. et al. The cytoplasm of living cells behaves as a poroelastic material. *Nat. Mater.* **12**, 253–261 (2013).
34. Guo, M. et al. Cell volume change through water efflux impacts cell stiffness and stem cell fate. *Proc. Natl Acad. Sci. USA* **114**, E8618–E8627 (2017).
35. Silverthorn, D. U., Johnson, B. R., Ober, W. C., Garrison, C. W. & Silverthorn, A. C. *Human Physiology: An Integrated Approach* Ch. 5 (Pearson Education, Boston, 2013).
36. Wakatsuki, T., Schwab, B., Thompson, N. C. & Elson, E. L. Effects of cytochalasin D and latrunculin B on mechanical properties of cells. *J. Cell Sci.* **114**, 1025–1036 (2001).
37. Salbreux, G., Charras, G. & Paluch, E. Actin cortex mechanics and cellular morphogenesis. *Trends Cell Biol.* **22**, 536–545 (2012).
38. Spector, I., Shorlet, N. R., Blasberger, D. & Kashman, Y. Latrunculins—novel marine macrolides that disrupt microfilament organization and affect cell growth: I. Comparison with cytochalasin D. *Cell Motil. Cytoskeleton* **13**, 127–144 (1989).
39. Morton, W. M., Ayscough, K. R. & Mclaughlin, P. J. Latrunculin alters the actin-monomer subunit interface to prevent polymerization. *Nat. Cell Biol.* **2**, 376–378 (2000).
40. Guck, J. & Chilver, E. R. Mechanics meets medicine. *Sci. Transl. Med.* **5**, 3–6 (2013).
41. Finan, J. D. & Guilak, F. The effects of osmotic stress on the structure and function of the cell nucleus. *J. Cell. Biochem.* **109**, 460–467 (2010).
42. Hallows, K. R., Packman, C. H. & Knauf, P. A. Acute cell volume changes in anisotonic media affect F-actin content of HL-60 cells. *Am. J. Physiol.* **261**, C1154–C1161 (1991).
43. Maruyama, K., Kaibara, M. & Fukada, E. Rheology of F-actin I. Network of F-actin in solution. *Biochim. Biophys. Acta Protein Struct.* **371**, 20–29 (1974).
44. Janmey, P. A., Euteneuer, U., Traub, P. & Schliwa, M. Viscoelastic properties of vimentin compared with other filamentous biopolymer networks. *J. Cell Biol.* **113**, 155–160 (1991).
45. Burg, T. P. et al. Weighing of biomolecules, single cells and single nanoparticles in fluid. *Nature* **446**, 1066–1069 (2007).
46. Nawaz, A. A. et al. Using real-time fluorescence and deformability cytometry and deep learning to transfer molecular specificity to label-free sorting. Preprint at *bioRxiv* <https://doi.org/10.1101/862227> (2019).
47. Rosendahl, P. et al. Real-time fluorescence and deformability cytometry. *Nat. Methods* **15**, 355–358 (2018).
48. Mietke, A. et al. Extracting cell stiffness from real-time deformability cytometry: theory and experiment. *Biophys. J.* **109**, 2023–2036 (2015).
49. Mokbel, M. et al. Numerical simulation of real-time deformability cytometry to extract cell mechanical properties. *ACS Biomater. Sci. Eng.* **3**, 2962–2973 (2017).
50. Fregin, B. et al. High-throughput single-cell rheology in complex samples by dynamic real-time deformability cytometry. *Nat. Commun.* **10**, 415 (2019).
51. Guck, J. Some thoughts on the future of cell mechanics. *Biophys. Rev.* **11**, 667–670 (2019).

Publisher's note Springer Nature remains neutral with regard to jurisdictional claims in published maps and institutional affiliations.

© The Author(s), under exclusive licence to Springer Nature America, Inc. 2020

Methods

Cell culture. The HL60/S4 cell subline (RRID: CVCL_I177; received from D. E. Olins and A. L. Olins, University of New England) was cultured in ATCC-modified RPMI 1640 medium (Gibco) with 1% penicillin and streptomycin (Gibco) and 10% heat-inactivated fetal bovine serum (Sigma Aldrich, catalog no. F4135, lot no. 13C519). Cells were grown at 37 °C, with 5% CO₂, at densities between 10⁵ and 10⁶ cells per ml with subculturing every second day. The cell line stocks were shared between the three participating laboratories at the same initial passage number and were used within ten passages upon receipt.

Osmotic shock. The measured osmolarity of the cell culture media and measurement buffers was 300 mOsm (Fiske 210 Micro-Sample Osmometer, Advanced Instruments). Hyperosmotic media were prepared by adding 182.2, 364.3, 546.5 and 728.6 mg of D-mannitol (Sigma Aldrich, MW 182.172 g mol⁻¹) per 10 ml of the appropriate measurement buffer to obtain solutions of 400, 500, 600 and 700 mOsm, respectively. Hypo-osmotic media were prepared by adding one part of deionized H₂O to two or five parts of the measurement buffer, to obtain a solution of 200 or 250 mOsm, respectively. HL60 cells at a density between 0.5 × 10⁶ and 1.0 × 10⁶ ml⁻¹ were centrifuged at 180g for 5 min and resuspended in osmolarity-adjusted measurement buffer. Cells were then incubated for 10 min at 37 °C and 5% CO₂ before measurement. The subsequent deformability measurements were conducted at room temperature (22–24 °C).

LatB treatment. Latrunculin B (Sigma Aldrich, MW 395.5 g mol⁻¹, catalog no. L5288) stock solution was prepared by dissolving the powder in DMSO at a concentration of 1 mg ml⁻¹ and the same stock solution was shared between the participating laboratories. The stock solution was further diluted in DMSO to 10,000× the desired concentration, to achieve equal DMSO concentration in all treatments (0.01% v/v). Subsequently, LatB was diluted 10,000× in the appropriate measurement buffer to final LatB concentrations of 1, 5, 10, 25, 50 and 100 ng ml⁻¹. HL60 cells at a density between 0.5 × 10⁶ and 1.0 × 10⁶ ml⁻¹ were collected by centrifugation at 180g for 5 min, resuspended in LatB-containing solution and incubated for 30 min at 37 °C and 5% CO₂ before measurement. The subsequent deformability measurements were conducted at room temperature (22–24 °C).

cDC measurements. The SMR used in this manuscript consisted of a 6 μm wide, 50 μm long and 15 μm deep constricted fluidic channel. Device dimensions and fabrication were similar to those described previously⁷. However, the device used in this study (fabricated by CEA-Leti) operated via piezoceramic actuation and had a piezoresistive readout system to monitor cantilever vibration frequency, which is similar to other types of SMR devices published previously^{52,53}. Before each experiment, channel walls were passivated with 1 mg ml⁻¹ polyethylene glycol (SuSoS, PLL(20)-g[3.5]-PEG(2)). The applied pressure differential driving the fluid flow through the system remained constant at 1.0 kPa for each experiment. Single-cell buoyant mass and passage time were determined from changes in the resonant frequency of the microcantilever. Individual cell diameters were determined by assuming a spherical shape for each cell, with its volume obtained by combining SMR buoyant mass measurements with Coulter counter volume measurements (Multisizer 4, Beckman Coulter) as described previously⁷.

sDC measurements. The production of the polydimethylsiloxane (PDMS) chip used for sDC measurements was performed according to previously described procedures⁵⁴. The experimental procedure for sDC measurements is described in detail elsewhere¹⁵. In brief, cells were suspended in a viscosity-adjusted measurement buffer (phosphate saline buffer without Mg²⁺ and Ca²⁺ (PBS-) containing 0.5% (w/v) methylcellulose; adjusted in HAAKE Falling Ball Viscometer type C (ThermoFisher Scientific) using ball number 3 to a viscosity of 15 mPa s, which corresponds to a viscosity of 5.7 mPa s at the measurement conditions⁵⁵) and introduced to the device via a syringe pump. The overall flow rate during the experiments was equal to 0.04 μl s⁻¹ (0.01 μl s⁻¹ sample flow together with 0.03 μl s⁻¹ focusing sheath flow) unless indicated otherwise. The imaging was performed at the end of a ~300-μm-long channel with a 20 × 20 μm² square cross-section with a high-speed camera at 2,000 frames per second and stroboscopic illumination with a pulse duration <3 μs to avoid motion blurring. The cell area and deformation were determined from cell contours in real time by an image-processing algorithm developed in-house⁴. Cell diameter was calculated during offline analysis from measured surface area and defined as for a circle with an equivalent surface area. To discard events with rough or incomplete contours, the results were filtered for an area ratio between 1.00 and 1.05. Area ratio is the ratio between the area enclosed by the convex hull of the cell contour and the raw area enclosed by the contour.

xDC measurements. The xDC microfluidic device has been previously described¹¹. Conventional soft lithography was used to fabricate the PDMS devices, which were then bonded to glass slides. Cell suspensions were injected via a syringe pump at 750 μl min⁻¹ into the microfluidic device with channel dimensions of 60 × 30 μm². The region surrounding the cross-slot channel was imaged with a high-speed bright-field camera at approximately 500,000 frames per second, with submicrosecond exposure time. Videos were automatically analyzed by a

MATLAB program that measures cell diameter before deformation and cell aspect ratio while deforming the cells. Cell diameter is defined as the minimum cell diameter in the direction perpendicular to flow ±30° before arrival of the cell at the cross-slot junction.

RD calculation. RD expresses the deformability of the treated cells, D_t , normalized to the median deformability of cells in the control condition for a given experimental series, \bar{D}_{ctrl} , according to the following formula: $RD = \frac{D_t}{\bar{D}_{ctrl}}$. Since the magnitude of deformability can be influenced by the cell size, RD calculations were based only on cells contained within the same 1-μm-wide diameter bin that was most represented among all treatment and control samples for a given experimental set (Supplementary Figs. 3 and 6). This procedure facilitates the assessment of the effects of a treatment on deformability, independent of the effect on cell size. The influence of the bin selection on the observed trends is illustrated in Supplementary Figs. 10 and 11.

Osmolarity data curve fitting. The response of cells to an osmotic shock is a dynamic process and, after initial cell swelling or shrinking, cells are known to undergo a regulatory volume response⁵⁶. Using sDC, we observed the response of cells between 2 and 30 min after exposure to osmotic shock. In the case of the hyperosmotic shock, the deformability and cell size decrease saturated in the first few minutes, whereas for the hypo-osmotic shock, deformability and cell size values initially increased, but then began to slowly return to their original values (Supplementary Fig. 4). Therefore, the values obtained for hypo-osmotic shock at the fixed 10-min measurement time were not included in the fitting procedure. The effect of normalized osmolarity, Osm/Osm_{iso} , on RD for hypertonic conditions was fit with: (1) exponential, (2) power law and (3) linear functions, adjusted to pass through a fixed point (1,1) representing control measurement at the isotonic osmolarity, Osm_{iso} . The fitting was performed using the nonlinear least-square nls function from the stats package in R (R Development Core Team). The goodness of different fits was assessed by evaluating their mean absolute residuals and Bayesian information criterion (BIC function in stats package in R). Exponential fit curves were compared in pairs via the F -test in R⁵⁷. To account for multiple pairwise comparison across the three datasets, Bonferroni-adjusted P values were calculated by multiplying P values by three⁵⁸.

LatB dose–response curve fitting. RD values calculated with respect to DMSO vehicle control for different LatB concentrations were used to fit a four-parameter log-logistic regression curve with the following formula⁵⁹:

$$RD([LatB], (b, c, d, e)) = c + \frac{d - c}{1 + \exp(b(\log([LatB]) - \log(e)))}$$

where [LatB] is the concentration of the drug, and b, c, d, e are the fit parameters, denoting: b , the steepness of the dose–response curve; c, d , the lower and upper limits of the response; e , the effective EC₅₀ dose at which half-maximum response is obtained. The fitting was performed using the drc function in the drc package⁵⁹ in R (R Development Core Team). Fit curves were compared in pairs via the F -test in R⁵⁷. To account for multiple pairwise comparison across the three datasets, Bonferroni-adjusted P values were calculated by multiplying P values by three⁵⁸.

Reporting Summary. Further information on research design is available in the Nature Research Reporting Summary linked to this article.

Data availability

Source data for Figs. 1–3 are provided alongside the manuscript. The dataset containing numerical values from all deformability measurements supporting findings of this study is available on figshare⁶⁰.

Code availability

MATLAB and R codes used to perform statistical analysis and generate data representations shown in this manuscript are available on GitHub at <https://github.com/dicarlo-lab/metadeforability>.

References

- Lee, J. et al. Suspended microchannel resonators with piezoresistive sensors. *Lab Chip* **11**, 645–651 (2011).
- Cermak, N. et al. High-throughput measurement of single-cell growth rates using serial microfluidic mass sensor arrays. *Nat. Biotechnol.* **34**, 1052–1059 (2016).
- Herbig, M. et al. in *Flow Cytometry Protocols. Methods in Molecular Biology* Vol. 1678 (eds Hawley, T. & Hawley, R.) 347–369 (Humana Press, 2018).
- Herold, C. Mapping of deformation to apparent Young's modulus in real-time deformability cytometry. Preprint at <http://arxiv.org/abs/1704.00572> (2017).
- Hoffmann, E., Lambert, I. H. & Pedersen, S. F. Physiology of cell volume regulation in vertebrates. *Physiol. Rev.* **89**, 193–277 (2009).

57. Motulsky, H. & Christopoulos, A. *Fitting Models to Biological Data Using Linear and Nonlinear Regression: A Practical Guide to Curve Fitting* Ch. F.22, 138–142 (Oxford Univ. Press, 2004).
58. Abdi, H. in *Encyclopedia of Measurement and Statistics* (ed. Salkind, N.) 103–107 (Sage, 2007).
59. Ritz, C., Baty, F., Streibig, J. C. & Gerhard, D. Dose-response analysis using R. *PLoS ONE* **10**, e0146021 (2015).
60. Urbanska, M. et al. MetaDeformability Dataset (Figshare, 2020); <https://doi.org/10.6084/m9.figshare.11704119>

Acknowledgements

We thank P. Janmey for helpful discussions, J. H. Kang and D. Soteriou for useful comments on the manuscript, A. Mietke (Massachusetts Institute of Technology) and C. Herold (Zellmechanik Dresden) for sharing parts of analysis codes, A.L. and D.E. Olins (University of New England) for providing the HL60/S4 cell line and the Microstructure Facility at the Center for Molecular and Cellular Bioengineering at Technische Universität Dresden (in part funded by the State of Saxony and the European Regional Development Fund) for help with the production of sDC chips. We acknowledge funding from the Alexander von Humboldt-Stiftung (Alexander von Humboldt Professorship to J.G.), the Ludwig Center for Molecular Oncology (S.R.M.), the Cancer Systems Biology Consortium U54 CA217377 and the Koch Institute Support Grant P30 CA14051 from the NCI (S.R.M.), the German Federal Ministry of Research and Education (ZIK grant to O.O. under grant agreement 03Z22CN11), and a Presidential Early Career Award for Scientists and Engineers (N00014-16-1-2997, to D.D.).

Author contributions

J.G., D.D. and S.R.M. conceptualized the project. M.U., H.E.M. and J.S.B. performed the experiments and analyzed the data. O.O. provided methodological support with sDC data acquisition and analysis. M.U. and H.E.M. visualized the data and prepared the original manuscript draft. All authors revised and edited the manuscript. J.G., D.D., S.R.M. and O.O. acquired funding.

Competing interests

M.U., H.E.M., J.S.B. and J.G. declare no competing interests. O.O. is a shareholder of Zellmechanik Dresden GmbH distributing real-time deformability cytometry; Zellmechanik Dresden GmbH owns a patent for Real-Time Deformability Cytometry (RT-DC): EU patent under the number EP 30 036 520 B1. S.R.M. is a founder of Travera and Affinity Biosensors. D.D. has financial interests in Cytovale Inc., which is commercializing deformability cytometry technology.

Additional information

Supplementary information is available for this paper at <https://doi.org/10.1038/s41592-020-0818-8>.

Correspondence and requests for materials should be addressed to S.R.M., D.D. or J.G.

Peer review information Nina Vogt was the primary editor on this article and managed its editorial process and peer review in collaboration with the rest of the editorial team.

Reprints and permissions information is available at www.nature.com/reprints.